

NANO EXPRESS

Open Access



Synthesis of MoIn_2S_4 @CNTs Composite Counter Electrode for Dye-Sensitized Solar Cells

Gentian Yue^{1*} , Renzhi Cheng¹, Xueman Gao¹, Leqing Fan², Yangfan Mao³, Yueyue Gao¹ and Furui Tan^{1*}

Abstract

A ternary and composite MoIn_2S_4 @CNTs counter electrode (CE) with a hedgehog ball structure was synthesized by using a facile one-step hydrothermal method. The composite MoIn_2S_4 @CNTs film possesses large specific surface area through N_2 adsorption-desorption isotherms test, which is advantageous to adsorb more electrolyte and provide larger active contact area for the electrode. In addition, the composite MoIn_2S_4 @CNTs CE exhibits low charge transfer resistance and fine electrocatalytic ability made from a series of electrochemical tests including cyclic voltammetry, electrochemical impedance, and Tafel curves. Under optimal conditions, the DSSC based on the MoIn_2S_4 @CNTs-2 composite CE achieves an impressive power conversion efficiency as high as 8.38%, which remarkably exceeds that of the DSSCs with the MoIn_2S_4 CE (7.44%) and the Pt electrode (8.01%). The current work provides a simplified preparation process for the DSSCs.

Keywords: Counter electrode, Dye-sensitized solar cell, MoIn_2S_4 , Carbon nanotubes, Power conversion efficiency

Background

In recent decades, it is urgent to exploit and utilize renewable energy substituting the conventional fossil fuels with the severe energy shortage and environmental degradation increasing [1, 2]. Dye-sensitized solar cell (DSSC) has attracted wide-spread research by virtue of its environmental friendliness, facile preparation process, brilliant photovoltaic performance, and so on [3, 4]. The counter electrode (CE), as one of the significant components of a DSSC, plays the role of gathering electrons from external circuit and catalyzing the reduction reaction of I_3^- to I^- in the liquid electrolyte [5, 6]. Generally, ideal CE materials contain the merits of high electrical conductivity and remarkable catalytic activity. However, platinum (Pt) as a prevalent and efficient CE material is confined to large-scale commercialized application because of the major weaknesses of scarcity, expensiveness,

and poorly long-term stability [7, 8]. Therefore, a great many of efforts have been made to develop easily accessible, cost-effective, and Pt-like catalytic activity applied in DSSC for years [9].

Up to now, various kinds of outstanding alternative materials have been proposed, such as carbonaceous materials [10, 11], transition metal chalcogenides [12], conductive polymers [13], metal alloys [14], and their compounds [15, 16]. Among them, the binary transition metal chalcogenides attracted a great deal of attention due to their unique structure and chemical properties. For instance, the synthesized MoS_2 on FTO substrate exhibits a sandwich-layered structure, larger surface area, and more active edge sites leading to extremely photoelectric performance as a CE for DSSC [17]. Meanwhile, extensive research work focused on the catalytic activity for I_3^- reduction also has been made for WS_2 [18], FeS_2 [19], CoS [20], and NiS_2 [21], which were comparable to or even better than that of the Pt electrode. Nevertheless, the inherent characteristic of these materials, such as low electrical conductivity and only

* Correspondence: yuegentian@126.com; fritan@henu.edu.cn

¹Henan Key Laboratory of Photovoltaic Materials and Laboratory of Low-Dimensional Materials Science, Henan University, Kaifeng 475004, People's Republic of China

Full list of author information is available at the end of the article

two-fixed chemical compositions, hampered further improvement in their catalytic activity [22]. Hence, numerous methods aimed to overcome the abovementioned shortcoming were adopted to synthesize multinary transition metal chalcogenides by component elements adjusting, structure designing, and morphology tailoring. Fortunately, considerable multinary transition metal chalcogenides have achieved significant enhancements in catalytic ability for DSSCs, such as NiCo_2S_4 [23], MIn_2S_4 ($\text{M} = \text{Fe}, \text{Co}, \text{Ni}$) [22], CuInS_2 [24], CoCuWS_x [25], and Ag_8GeS_6 [26], which catalytic ability are obviously much better than that of their binary counterparts.

Moreover, it is widely acknowledged that carbon nanotubes (CNTs) exhibit considerably novel characteristics of large specific surface area, superb electrical conductivity, high mechanical strength, and photochemical stability, which are widely used in the synthesis and modification of other materials [27]. Regrettably, CNTs show poor electrocatalytic activity for I_3^- reduction, which greatly limits their application independently in a DSSC device. Fortunately, a large number of studies have shown that the composite CE modified with CNTs all obtained greatly improved photoelectric performance for DSSCs [18, 28, 29]. Liu et al. have reported a flower-like hierarchical structure of $\text{Cu}_2\text{MnSnS}_4/\text{CNT}$ (CMTS/CNT) CE via solvothermal method in DSSC gained a photoelectric conversion efficiency of 8.97%, much higher than that of the DSSCs with CMTS (6.21%) and Pt (8.37%) CEs [29].

Based on the above considerations, in this study, a $\text{MoIn}_2\text{S}_4/\text{CNT}$ composite CE of DSSC with hedgehog ball structure was synthesized by using a facile one-step hydrothermal method and expected to improve higher device performance. Scanning electron microscope results show that different CNT contents result in visible changes on morphology. According to a series of electrochemical characterizations including cyclic voltammetry (CV), electrochemical impedance spectroscopy (EIS), and Tafel curves tests, the $\text{MoIn}_2\text{S}_4/\text{CNTs}$ CE indicates a remarkable catalytic activity and fine charge transfer resistance. The DSSC assembled with the $\text{MoIn}_2\text{S}_4/\text{CNTs}$ CE with suitable content achieves a superior power conversion efficiency of 8.38%, which is better than that of the DSSC based on the Pt CE (8.01%).

Methods

Materials

Sodium molybdate dihydrate ($\text{Na}_2\text{MoO}_4 \cdot 2\text{H}_2\text{O}$), indium chloride tetrahydrate ($\text{InCl}_3 \cdot 4\text{H}_2\text{O}$), and thioacetamide (TAA) were purchased from Shanghai Chemical Agent Ltd., China, which were used directly without further purification. Carbon nanotubes (CNTs) were gained from Aladdin Chemical Agent Ltd., China. The

commercial Z907 dye was obtained from Solaronix Ltd. (Switzerland). The fluorine-doped SnO_2 (FTO) glass, purchased from NSG, Japan ($15 \Omega \text{ sq}^{-1}$), were cleaned with detergent and acetone as well as ethyl alcohol in sequence after cutting into squares of $1.5 \text{ cm} \times 2.0 \text{ cm}$.

Preparation of porous TiO_2 photoanodes

The colloid of TiO_2 was prepared as our previous work [30]. The dye-sensitized TiO_2 photoanodes were fabricated as follows: Firstly, 3-M tape ($50 \mu\text{m}$ thick) with exposed area of 0.283 cm^2 was attached on FTO. Subsequently, the as-prepared TiO_2 colloid was coated on by using a blade-coating method. Secondly, the drying TiO_2 electrode was sintered at 450°C for 30 min in muffle furnace. Afterwards, the TiO_2 electrode was immersed in a 40-mM titanium tetrachloride (TiCl_4) aqueous solution at 70°C for 30 min, and then annealed in air at 450°C for 30 min. After cooling down to room temperature, the TiO_2 electrode was immersed in dye Z907 (0.3 mM) absolute ethanol solution for 24 h to adsorb sufficient dyes and obtained the resultant dye-sensitized TiO_2 photoanode.

Fabrication of ternary $\text{MoIn}_2\text{S}_4/\text{CNTs}$ CE

The MoIn_2S_4 thin films were grown directly onto FTO substrates by a simple approach referring to our previous report [31]. In a typical preparation, 0.0696 g $\text{Na}_2\text{MoO}_4 \cdot 2\text{H}_2\text{O}$, 0.169 g $\text{InCl}_3 \cdot 4\text{H}_2\text{O}$, and 0.1394 g TAA were diffused in 30 ml deionized water under ultrasonication for 2 h until all the reactants were dissolved. The pre-cleaned FTO substrates were put into a 100-ml Teflon-lined stainless steel autoclave with the conductive side facing up before transferring the above precursor mixture into it. After being sealed, the autoclave was placed in an oven and heated under 200°C for a reaction time of 15 h. The FTO glass substrates covered with MoIn_2S_4 materials were taken out from the autoclave, washed with ethanol, deionized water, and then dried in air under 60°C for 12 h.

In order to study the impact of the CNT contents on the fabricated composite CE and the performance of the DSSC, different contents of CNTs adding to the precursor were conducted, including three samples in which the amount of CNTs were 10, 20, and 30 mg, respectively, keeping the other reagents and fabrication processes unchanged. The above samples were marked MoIn_2S_4 (0 mg), $\text{MoIn}_2\text{S}_4/\text{CNTs-1}$ (10 mg), $\text{MoIn}_2\text{S}_4/\text{CNTs-2}$ (20 mg), and $\text{MoIn}_2\text{S}_4/\text{CNTs-3}$ (30 mg).

For comparison, a pyrolysed Pt CE was employed as the reference CE. The H_2PtCl_6 in isopropanol solution (0.50 wt%) was dropped onto the surface of the FTO glass, and then sintered at 450°C in muffle furnace for 30 min to fabricate the Pt CE.

Fabrication of the DSSCs

The DSSCs with sandwich structure were constructed by clipping the sample CEs (including MoIn_2S_4 , various $\text{MoIn}_2\text{S}_4@\text{CNTs}$, and Pt CEs) together with as-prepared dye-sensitized TiO_2 photoanode. Surlyn was used as spacer between the electrodes and followed by filling the interspace with liquid redox electrolyte that consisted of 0.60 M tetrabutylammonium iodide, 0.10 M lithium iodide, 0.05 M iodine, and 0.50 M 4-tert-butyl-pyridine acetonitrile solution.

Characterizations

Chemical element composition of the samples was characterized by using X-ray photoelectron spectroscopy (XPS) analysis (Kratos Axis Ultra). The morphological features of samples were observed by field emission scanning electron microscopy (FESEM, JSM-7001F). BET-specific surface area method was employed using a JW-K analyser by nitrogen absorption to test the surface area and pore size distribution. The other relevant electrochemical properties were researched by a CHI660E electrochemical workstation. The electrochemical impedance spectroscopy (EIS) was performed in a frequency range of 0.1– 10^5 Hz with a disturbed amplitude of 5 mV. The photovoltaic performances of the DSSCs were carried out by measuring current density-voltage

(J - V) characteristic curves under irradiation of 100 mW cm^{-2} from the solar simulator (CEL-S500, Beijing China Education Au-light Co., Ltd).

Results and Discussions

Composition and Morphology

The XPS is employed to examine the surface compositions and chemical states of each element in MoIn_2S_4 and $\text{MoIn}_2\text{S}_4@\text{CNTs}$ films. The spectrum of survey data in MoIn_2S_4 and $\text{MoIn}_2\text{S}_4@\text{CNTs}$ -2 samples is demonstrated in Fig. 1a to verify the presence of Mo, In, S, and C (as a reference) elements. In addition, all spectra of the four samples, calibrated by the C 1s peak at the binding energy of 284.6 eV [17], are analyzed via the Gaussian fitting method showing in Fig. 1b and c. The C 1s peak appeared in MoIn_2S_4 sample is well known to have originated from the adventitious carbon caused by exposure to the air. In the Mo 3d region, two major peaks at 228.8 and 232.1 eV are assigned to Mo 3d_{5/2} and Mo 3d_{3/2} of the MoS_2 [32], respectively. This result confirms that Mo element is in its IV oxidation state, which is reduced to Mo^{4+} (MoIn_2S_4) from Mo^{6+} (Na_2MoO_4) [33]. The doublet peaks at binding energies of 445.2 and 452.2 eV correspond to In 3d_{5/2} and In 3d_{3/2} [24, 34]. As for the XPS spectra of S 2p, the peaks located at 161.8 and 163.1 eV belong to S 2p_{3/2} and

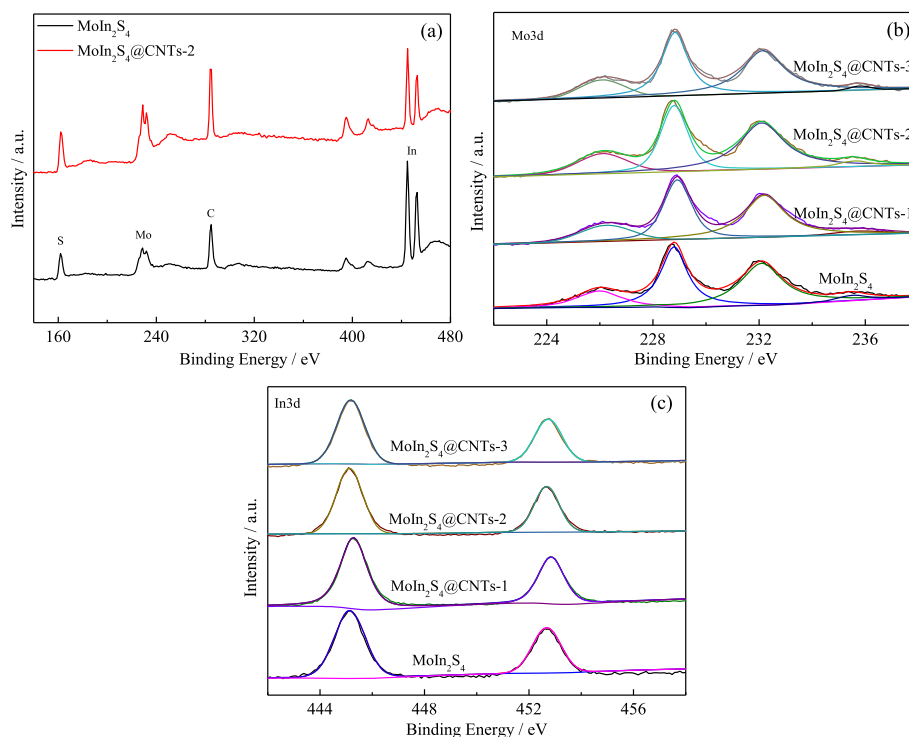


Fig. 1 XPS spectra of the samples.

Fig. 1 XPS spectra of the samples

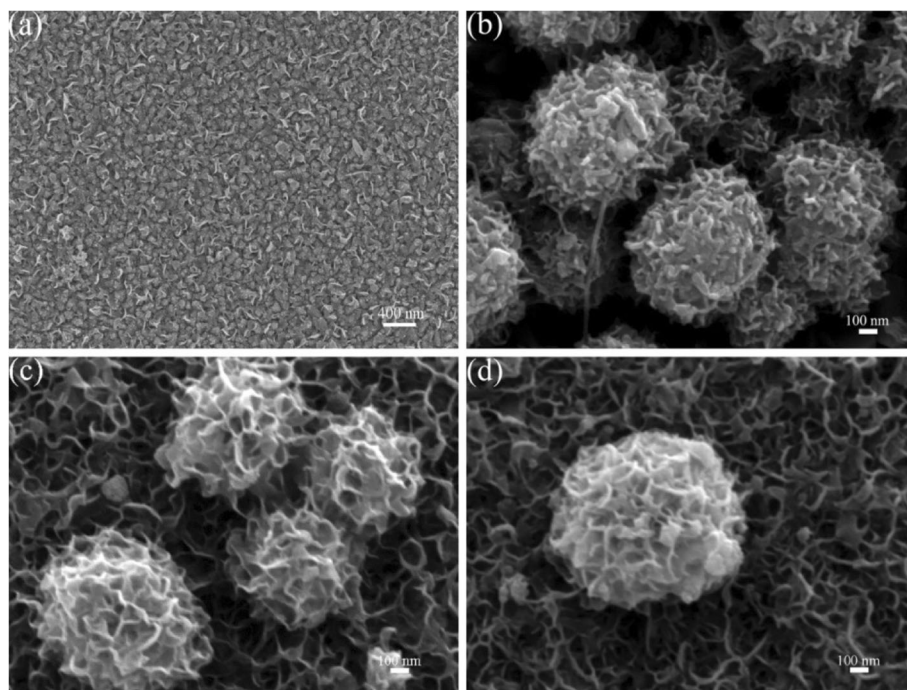


Fig. 2 SEM images of **a** MoIn₂S₄, **b** MoIn₂S₄@CNTs-1, **c** MoIn₂S₄@CNTs-2, and **d** MoIn₂S₄@CNTs-3

2p_{1/2}, respectively, which is ascribed to the S₂[−] [17, 32]. The above results are well in agreement with our previous studies [31]. Moreover, no other element or extra peak is found in the survey, which reconfirms that the samples synthesized have the similar chemical compositions and structure.

The surface morphologies of as-prepared MoIn₂S₄ and MoIn₂S₄@CNTs nanofilms are observed by SEM images in Fig. 2. In Fig. 2a, MoIn₂S₄ sample displays a petal-like nanosheet structure with a uniform, smooth, and dense surface. Unlike MoIn₂S₄ nanofilms, the hedgehog ball structure is found in MoIn₂S₄@CNT samples in Fig. 2b–d, and the average

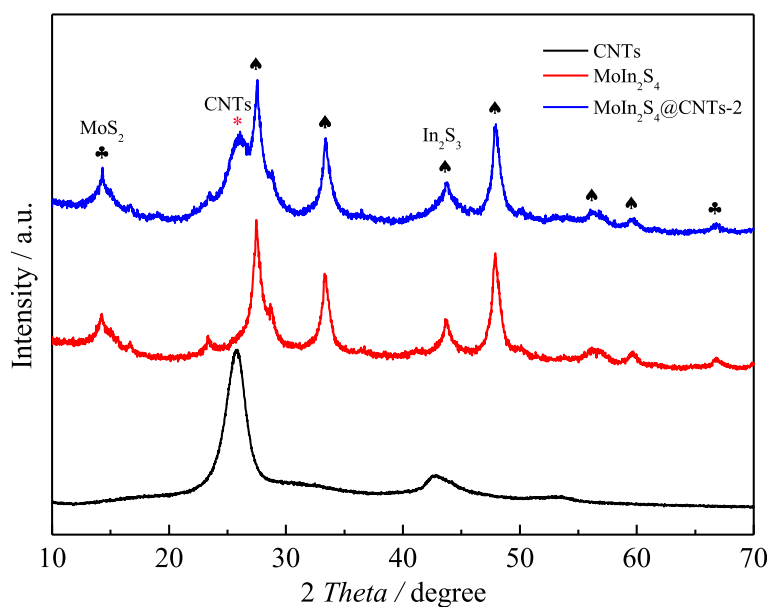


Fig. 3 XRD patterns of various samples

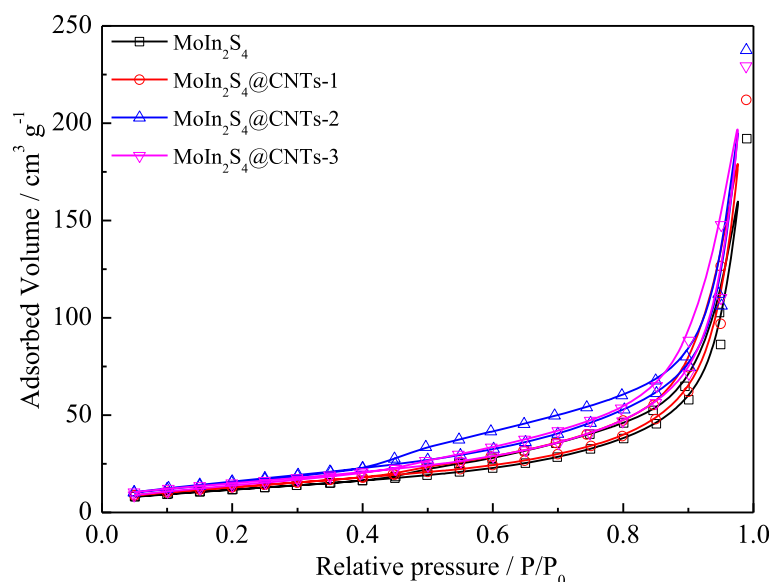


Fig. 4 N_2 adsorption-desorption isotherms of various samples

diameter of the $MoIn_2S_4@CNTs$ nanospheres is around 890 nm. It is easy to observe that so many network nanosheets are fully grown on the FTO substrate. Compared to the $MoIn_2S_4@CNT$ samples with low ($MoIn_2S_4@CNTs-1$) and high ($MoIn_2S_4@CNTs-3$) CNT contents, the sample with moderate content ($MoIn_2S_4@CNTs-2$) exhibits more hedgehog balls and nanosheets array on the network of the $MoIn_2S_4$. A good contact performance between the network nanosheet array structure with large number hedgehog balls on FTO substrate facilitates the reduction of I_3^- attributed to its good conductivity and vast catalytic active sites, which can be predicted that the $MoIn_2S_4@CNTs-2$ CE will achieve better performance than that of the $MoIn_2S_4$, $MoIn_2S_4@CNTs-1$, and $MoIn_2S_4@CNTs-3$ CEs. Moreover, dissimilar morphologies between $MoIn_2S_4$ and $MoIn_2S_4@CNTs$ indicate that CNTs play a pivotal role in controlling morphology of the samples.

Figure 3 shows the XRD patterns of various samples. Among them, the diffraction peaks at $2\theta = 25.74$ and 42.85° attribute to the signals of the CNTs [31]. The diffraction peaks at $2\theta = 27.5, 33.4, 43.7, 47.9, 56.2$, and 59.6° belong to the (311), (400), (511), (440), (533), and (444)

crystallographic plane (JCPDS card no. 32-0456) of In_2S_3 . The peaks at 14.4 and 66.5° are regarded to (002) and (114) crystal planes of cubic structure (JCPDS card no. 37-1492) for the MoS_2 [33]. From the $MoIn_2S_4@CNTs-2$ and $MoIn_2S_4$ samples, the peaks of the above discussed appear well in the both samples. Compared to the $MoIn_2S_4$ sample, the peak for the CNTs at 25.74° can be seen clearly in $MoIn_2S_4@CNTs-2$ XRD patterns. Thus, it can be inferred that the $MoIn_2S_4@CNTs-2$ materials are synthesized successfully and there are no impurities introduction.

N_2 adsorption-desorption isotherms are measured and showed in Fig. 4 to explore the specific surface areas and pore features. Generally, the larger specific surface area facilitates more convenient charge transmission on the CE/electrolyte interface [35]. It demonstrates from Fig. 4 that the samples possess an evident hysteresis loop of type IV adsorption-desorption behavior, and their corresponding data calculated from the Brunauer-Emmett-Teller (BET) and Barrett-Joyner-Halenda (BJH) method are tabulated in Table 1. By comparison, it is easy to find that the specific surface area and average pore diameter of the $MoIn_2S_4@CNT$ samples are much better than that of the $MoIn_2S_4$. Among the three $MoIn_2S_4@CNT$ samples, $MoIn_2S_4@CNTs-2$ shows the largest specific surface area of $66.80 \text{ m}^2 \text{ g}^{-1}$ and the smallest average pore diameter of 17.8 nm, which can be ascribed to the excellent hedgehog ball structure after doping of moderate CNTs. It is reasonable to believe that the $MoIn_2S_4@CNTs-2$ CE will obtain the fine catalytic activity and hence achieve highly efficient device performance.

Table 1 The parameters of N_2 absorption-desorption isotherms of various samples

CEs	$S_{BET} (\text{m}^2 \text{ g}^{-1})$	$d_A (\text{nm})$	$ j_{pc} (\text{mA cm}^{-2})$
$MoIn_2S_4$	44.27	35.9	4.31
$MoIn_2S_4@CNTs-1$	55.79	23.8	4.68
$MoIn_2S_4@CNTs-2$	66.80	17.8	7.47
$MoIn_2S_4@CNTs-3$	61.80	21.2	5.09

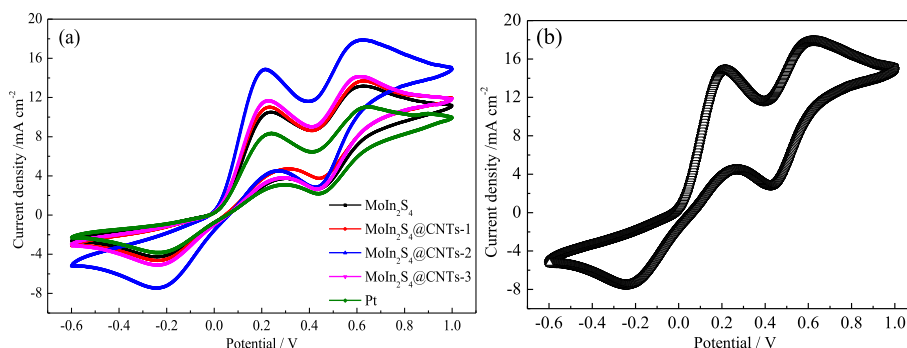


Fig. 5 **a** CVs of the various CEs at a scan rate of 60 mV s⁻¹. **b** 50 cycles CV of the MoIn₂S₄@CNTs-2 CE

Electrochemical properties

CV measurements are carried out to study the electrocatalytic behavior of the as-obtained samples in the potential range of -0.6 to 1.0 V at a scan rate of 60 mV s⁻¹ for the MoIn₂S₄ and MoIn₂S₄@CNTs CEs, and the calculated values are summed up in Table 1. The left peaks of the two pairs of oxidation and reduction peaks in each CV curve in Fig. 5a are ascribed to the equation ($I_3^- + 2e^- \leftrightarrow 3I^-$), which determines the performance of electrocatalytic activity of the CE materials, especially in DSSCs [23, 36]. The values of the negative reduction peak current density (J_{pc}), a key parameter in CV test, follows the orders of Pt (3.80 mA cm⁻²) < MoIn₂S₄

(4.31 mA cm⁻²) < MoIn₂S₄@CNTs-1 (4.68 mA cm⁻²) < MoIn₂S₄@CNTs-3 (5.09 mA cm⁻²) < MoIn₂S₄@CNTs-2 (7.47 mA cm⁻²). Evidently, the MoIn₂S₄ CE itself has good catalytic activity, and the MoIn₂S₄@CNTs-2 CE exhibits much higher J_{pc} than that of the Pt, MoIn₂S₄ CEs, and the other two kinds of MoIn₂S₄@CNTs CEs attributed to its distinctive surface morphology, the synergistic effect of CNTs doped, and the larger surface area. The results indicate that the MoIn₂S₄@CNTs-2 CE has fine electrocatalytic activity for the I^-/I_3^- redox couple in DSSC CEs. Figure 5b shows the CV curves of the MoIn₂S₄@CNTs-2 CE at the scan rate of 60 mV s⁻¹

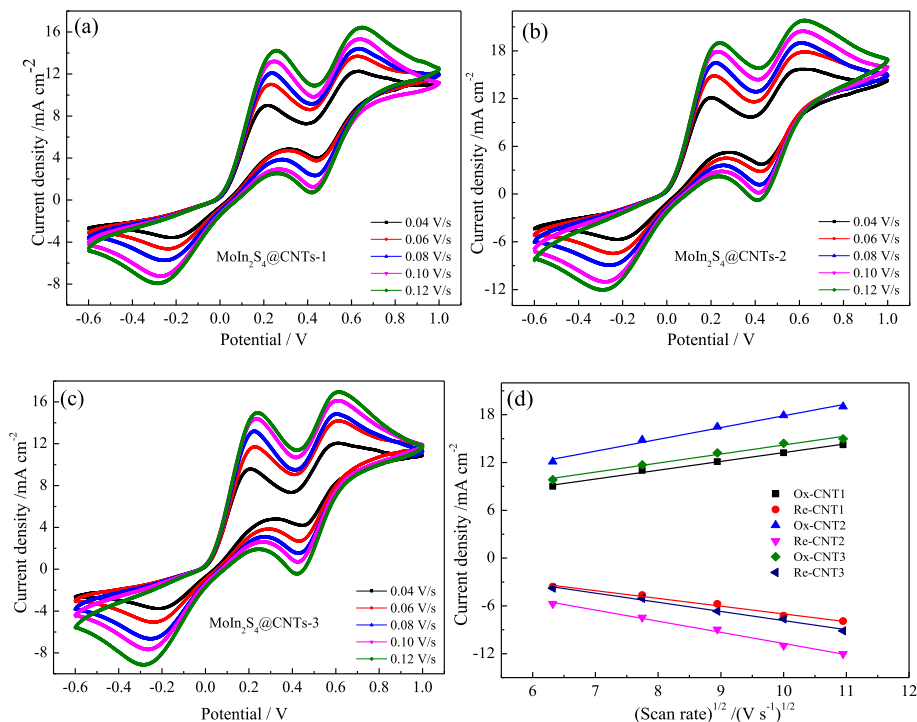


Fig. 6 CVs of the MoIn₂S₄@CNTs CEs at different scan rates **a** MoIn₂S₄@CNTs-1, **b** MoIn₂S₄@CNTs-2, **c** MoIn₂S₄@CNTs-3, and **d** the influences of the scan rate on the redox peaks current density

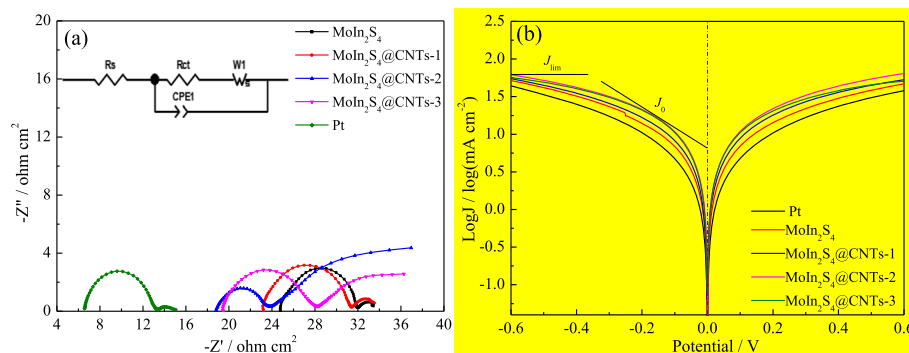


Fig. 7 **a** EIS and **b** Tafel curves of the symmetrical MoIn₂S₄, MoIn₂S₄@CNTs-1, MoIn₂S₄@CNTs-2, and MoIn₂S₄@CNTs-3 CEs

and they are almost no changing with 50 cycles, which indicates that the MoIn₂S₄@CNTs-2 CE possesses excellent electrochemical stability.

Figure 6a–c show the CVs of MoIn₂S₄@CNTs CEs at different scan rates. With the scan rates increasing from 20 to 120 mV s⁻¹, the oxidation and reduction peaks shift towards positive and negative direction owing to the fast diffusions of I⁻/I₃⁻ redox couple on the surfaces of CEs and the large electrochemical polarization [28]. Furthermore, Fig. 6d shows the relationship between the anodic and cathodic peak current densities of the left peak pairs against the square root of sweep rates. The well-fitted linear relations indicate that the redox reaction of I⁻/I₃⁻ is dominated by diffusion-controlled ion transport [22, 25].

Figure 7a shows the Nyquist plots of the different samples to further insight into the kinetics of the interfacial charge transfer process. The EIS data made from the fitted curves with a model equivalent circuit of the insert is listed in Table 2. Typically, the Nyquist plots contain two semicircles, the first semicircle on the left represents the charge transfer resistance R_{ct} at the CE and electrolyte interface, and the second semicircle corresponds to the Nernst diffusion impedance in the electrolyte, while the intercept of the curve in the high-frequency region on the real axis is known as the series resistance R_s . In general, R_s and R_{ct} are two vital parameters for evaluating the catalytic activity of CE in DSSC. A small R_s indicates good contact between the catalyst and the substrate, and hence the resistance of the entire device is also small [29, 37, 38]. Meanwhile, little R_{ct} stands for a

high charge transfer rate. As presented in Table 2, the R_s values of the MoIn₂S₄, MoIn₂S₄@CNTs-1, MoIn₂S₄@CNTs-2, and MoIn₂S₄@CNTs-3 CEs are 24.77, 23.16, 18.96, and 19.58 Ω cm², respectively. Obviously, all the composite MoIn₂S₄@CNTs CEs have the smaller R_s than that of the MoIn₂S₄ CE, indicating that the conductivity of the MoIn₂S₄@CNTs CEs is enhanced after doping CNTs. Furthermore, among the four CEs, the trends of R_{ct} is MoIn₂S₄ > MoIn₂S₄@CNTs-1 > MoIn₂S₄@CNTs-3 > MoIn₂S₄@CNTs-2, which suggests an inverse order of electrochemical impedance and catalytic ability of the CEs. MoIn₂S₄@CNTs-2 CE possesses the lowest R_{ct} value can be attributed to the synergy of the CNTs with fine conductivity and MoIn₂S₄ with excellent catalytic ability, resulting in more effective reduction of triiodide on the CE/electrolyte interface. Apparently, the conductivity and catalytic ability of the MoIn₂S₄@CNTs composite CEs has been improved greatly than that of the MoIn₂S₄ CE, and the result is completely consistent with the BET and CV tests.

The Tafel polarization curves of the various CEs are measured as shown in Fig. 7b, and the corresponding parameters values are summarized in Table 2. Normally, a standard Tafel curve includes two significant parameters named exchange current density (J_0) and limiting diffusion current density (J_{lim}). J_0 is related to the catalytic reduction reaction. The larger the J_0 is, the better the catalytic effect. J_{lim} is also positively related to the diffusion efficiency of electrolyte. The larger J_{lim} indicates the faster diffusion of I₃⁻ ions [29, 37]. As presented in Fig. 7b and Table 2, the J_{lim} and J_0 are all in

Table 2 Electrochemical parameters for the different CEs

Electrodes	R_s (Ω cm ²)	R_{ct} (Ω cm ²)	J_{lim} (mA cm ⁻²)	J_0 (mA cm ⁻²)
MoIn ₂ S ₄	24.77	7.291	1.67	1.11
MoIn ₂ S ₄ @CNTs-1	23.16	8.078	1.70	1.18
MoIn ₂ S ₄ @CNTs-2	18.96	3.162	1.81	1.35
MoIn ₂ S ₄ @CNTs-3	19.58	6.401	1.72	1.32
Pt	6.56	7.177	1.58	1.04

Table 3 Photovoltaic parameters of DSSCs

CEs	J_{sc} (mA cm ⁻²)	V_{oc} (V)	FF	η (%)
CNTs	12.57	0.745	0.387	3.62
MoIn ₂ S ₄	14.46	0.760	0.677	7.44
MoIn ₂ S ₄ @CNTs-1	16.31	0.744	0.672	8.16
MoIn ₂ S ₄ @CNTs-2	17.17	0.745	0.655	8.38
MoIn ₂ S ₄ @CNTs-3	16.67	0.773	0.644	8.31
Pt	15.48	0.754	0.686	8.01

orders of Pt < MoIn₂S₄ < MoIn₂S₄@CNTs-1 < MoIn₂S₄@CNTs-3 < MoIn₂S₄@CNTs-2, suggesting that the catalytic activity of the MoIn₂S₄@CNTs-2 CE has enhanced greatly after doping CNTs. Among above CEs, the MoIn₂S₄@CNTs-2 CE gains the best catalytic activity compared to the others. The largest J_{lim} and J_0 of the MoIn₂S₄@CNTs-2 CE can be ascribed to its large specific surface area made from hedgehog ball structure and enhanced conductivity by CNTs doping.

Photovoltaic performance of the DSSCs

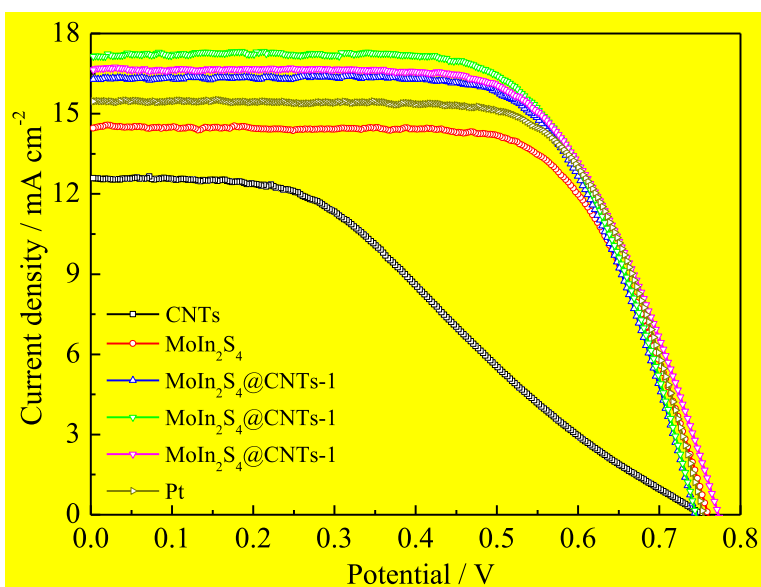
For contrast, the DSSCs with the MoIn₂S₄, MoIn₂S₄@CNTs, and Pt CEs are prepared with the uniform photoanodes and electrolyte. The J - V characteristic curves are measured under 1 sun (AM 1.5 G, 100 mW cm⁻²) and the corresponding photovoltaic parameters values are listed in Table 3. Four key parameters including short-circuit current density (J_{sc}), open-circuit voltage (V_{oc}), fill factor (FF), and power conversion efficiency (η) are usually adopted to assess the photovoltaic performance of the DSSCs. The FF and η of the DSSCs are calculated according to the Eqs. (1) and (2):

$$\eta (\%) = \frac{V_{max} \times J_{max}}{P_{in}} \times 100\% = \frac{V_{oc} \times J_{sc} \times FF}{P_{in}} \times 100\% \quad (1)$$

$$FF = \frac{V_{max} \times J_{max}}{V_{oc} \times J_{sc}} \quad (2)$$

where P_{in} is the incident light power and J_{max} (mA cm⁻²) and V_{max} (V) are the current density and voltage at the point of maximum power output in the J - V curves, respectively.

As can be seen from Fig. 8, the DSSCs with MoIn₂S₄ and CNTs CEs have power conversion efficiency of 7.44% and 3.62%. Compared to the DSSCs with the MoIn₂S₄ and CNTs CEs, the DSSCs assembled with the three MoIn₂S₄@CNTs CEs exhibit improvement J_{sc} and η values. Moreover, the J_{sc} and η values of the DSSCs based on the MoIn₂S₄@CNTs CEs increase with the CNT contents increasing from 10 to 20 mg. While further increases the CNT content to 30 mg, it results in a slight descent for the J_{sc} and η . Compared with the Pt-based DSSC, all the three MoIn₂S₄@CNTs-based DSSCs exhibit improved η of 8.16%, 8.31%, and 8.38%, which are higher than that of the Pt-based DSSC (η of 8.01%) under the same condition. Especially, the DSSC assembled with the MoIn₂S₄@CNTs-2 CE shows the best photovoltaic performance and achieves a η of 8.38%, and its corresponding J_{sc} of 17.17 mA cm⁻², V_{oc} of 0.745 V, and FF of 0.655. The improved photoelectric property of the DSSC with the MoIn₂S₄@CNTs-2 CE was due to the synergetic effect of the CNTs and the MoIn₂S₄.

**Fig. 8** J - V characteristics of the DSSCs fabricated with different CEs

Conclusions

Ternary MoIn_2S_4 and $\text{MoIn}_2\text{S}_4/\text{CNTs}$ counter electrodes are fabricated on FTO substrate by using a facile one-step hydrothermal method and served in DSSCs. Under optimal conditions, the DSSCs based on the $\text{MoIn}_2\text{S}_4/\text{CNTs}$ CE all achieve good power conversion efficiency. Especially, the DSSC with the $\text{MoIn}_2\text{S}_4/\text{CNTs}$ -2 composite CE exhibits a good power conversion efficiency of 8.38%, which is much higher than that of the DSSCs with the MoIn_2S_4 CE (7.44%) and the Pt electrode (8.01%). The enhanced photoelectric property of the DSSC with the $\text{MoIn}_2\text{S}_4/\text{CNTs}$ -2 CE was due to the synergetic effect of the CNTs and the MoIn_2S_4 . Meanwhile, the synergetic effect of the $\text{MoIn}_2\text{S}_4/\text{CNTs}$ CE in electrochemical performance has confirmed from a series of electrochemical test including cyclic voltammetry, electrochemical impedance, and Tafel curves. The composite $\text{MoIn}_2\text{S}_4/\text{CNTs}$ film possesses large specific surface area through N_2 adsorption-desorption isotherms test, which is advantageous to adsorb more electrolyte and provide larger active contact area for the electrode. The facts of the $\text{MoIn}_2\text{S}_4/\text{CNTs}$ CE served in DSSC broadens the potential applications of transition metal complex semiconductors in the field of optoelectronic chemistry.

Abbreviations

CE: Counter electrode; CV: Cyclic voltammetry; DSSC: Dye-sensitized solar cell; I^-/I_3^- : Iodide/triiodide; J_0 : Exchange current density; J_{lim} : Limiting current density; J_{max} : Maximum current density; J_{sc} : Short-circuit current density; $J-V$: Photocurrent-photovoltage; P_{in} : Incident light power; R_{ct} : Charge transfer resistance; R_s : Series resistance; SEM: Scanning electron microscopy; V_{max} : Maximum voltage; V_{oc} : Open-circuit voltage

Acknowledgements

The authors are very grateful to the joint support by NSFC (No. 61704047). This work is also supported by open topic of Fujian Key Laboratory of Photoelectric Functional Materials (FJPFM-201501).

Authors' Contributions

RC carried out the experiments, participated in the sequence alignment, and drafted the manuscript. XG participated in the device preparation. LF, MY, and YG were involved in the SEM, EIS, and CV analysis of the devices. GY and FT were responsible to draft the manuscript. All authors read and approved the final manuscript.

Availability of Data and Materials

All data sets on which the conclusions of the manuscript rely are presented in the main paper.

Competing Interests

The authors declare that they have competing interests.

Author details

¹Henan Key Laboratory of Photovoltaic Materials and Laboratory of Low-Dimensional Materials Science, Henan University, Kaifeng 475004, People's Republic of China. ²Fujian Key Laboratory of Functional Materials, Huaqiao University, Xiamen 361021, Fujian, People's Republic of China. ³School of Chemical Engineering and Materials Science, Quanzhou Normal University, Quanzhou 362000, People's Republic of China.

Received: 15 July 2020 Accepted: 14 September 2020

Published online: 21 September 2020

References

- Dresselhaus MS, Thomas IL (2001) Alternative energy technologies. *Nature* 414:332–337
- Balzani V, Credi A, Venturi M (2008) Photochemical conversion of solar energy. *ChemSusChem* 1:26–58
- O'Regan B, Grätzel M (1991) A low-cost, high-efficiency solar cell based on dye-sensitized colloidal TiO_2 films. *Nature* 353:737–740
- Hagfeldt A, Boschloo G, Sun L, Kloo L, Pettersson H (2010) Dye-sensitized solar cells. *Chem Rev* 110:6595–6663
- Wu JH, Lan Z, Lin JM, Huang ML, Huang YF, Fan LQ, Luo GG, Lin Y, Xie YM, Wei YL (2017) Counter electrodes in dye-sensitized solar cells. *Chem Soc Rev* 46:5975–6023
- Thomas S, Deepak TG, Anjusree GS, Arun TA, Nair SV, Nair AS (2014) A review on counter electrode materials in dye-sensitized solar cells. *J Mater Chem A* 2:4474–4490
- Theerthagiri J, Senthil AR, Madhavan J, Maiyalagan T (2015) Recent progress in non-platinum counter electrode materials for dye-sensitized solar cells. *ChemElectroChem* 2:928–945
- Briscoe J, Dunn S (2016) The future of using earth-abundant elements in counter electrodes for dye-sensitized solar cells. *Adv Mater* 28:3802–3813
- Yun SN, Hagfeldt A, Ma TL (2014) Pt-free counter electrode for dye-sensitized solar cells with high efficiency. *Adv Mater* 26:6210–6237
- Zhou ZP, Sigdel S, Gong JW, Vaagensmith B, Elbohy H, Yang HJ, Krishnan S, Wu XF, Qiao QQ (2016) Graphene-beaded carbon nanofibers with incorporated Ni nanoparticles as efficient counter electrode for dye-sensitized solar cells. *Nano Energy* 22:558–563
- Yun SN, Hou YZ, Wang C, Zhang YL, Zhou X (2019) Mo_2C -based binary and ternary nanocomposites as high-efficiency counter electrodes for dye-sensitized solar cells. *Ceram Int* 45:15589–15595
- Singh E, Kim KS, Yeom GY, Nalwa HS (2017) Two-dimensional transition metal dichalcogenide-based counter electrodes for dye-sensitized solar cells. *RSC Adv* 7:28234–28290
- Xiao YM, Lin JY, Tai SY, Chou SW, Yue GT, Wu JH (2012) Pulse electropolymerization of high performance PEDOT/MWCNT counter electrodes for Pt-free dye-sensitized solar cells. *J Mater Chem* 22:19919–19925
- Chang PJ, Cheng KY, Chou SW, Shyue JJ, Yang YY, Hung CY, Lin CY, Chen HL, Chou HL, Chou PT (2016) Tri-iodide reduction activity of shape- and composition-controlled PtFe nanostructures as counter electrodes in dye-sensitized solar cells. *Chem Mater* 28:2119–2129
- Lou Y, Zhao WJ, Li CG, Huang H, Bai TY, Chen CL, Liang C, Shi Z, Zhang D, Chen XB, Feng SH (2017) Application of $\text{Cu}_3\text{InSnS}_5$ heteronanostructures as counter electrodes for dye-sensitized solar cells. *ACS Appl Mater Interfaces* 9:18046–18053
- Sigdel S, Dubey A, Elbohy H, Aboagye A, Galipeau D, Zhang L, Fong H, Qiao QQ (2014) Dye-sensitized solar cells based on spray-coated carbon nanofiber/ TiO_2 nanoparticle composite counter electrodes. *J Mater Chem A* 2:11448–11453
- Liang J, Li J, Zhu HF, Han YX, Wang YR, Wang CX, Jin Z, Zhang GM, Liu J (2016) One-step fabrication of large-area ultrathin MoS_2 nanofilms with high catalytic activity for photovoltaic devices. *Nanoscale* 8:16017–16025
- Wu JH, Yue GT, Xiao YM, Huang ML, Lin JM, Fan LQ, Lan Z, Lin JY (2012) Glucose aided preparation of tungsten sulfide/multi-wall carbon nanotube hybrid and sse as counter electrode in dye-sensitized solar cells. *ACS Appl Mater Interfaces* 4:6530–6536
- Wang YC, Wang DY, Jiang YT, Chen HA, Chen CW (2013) FeS_2 nanocrystal ink as a catalytic electrode for dye-sensitized solar cells. *Angew Chem Int Ed* 52:6694–6698
- Kung CW, Chen HW, Lin CY, Huang KC, Vittal R, Ho KC (2012) CoS acicular nanorod arrays for the counter electrode of an efficient dye-sensitized solar cell. *ACS Nano* 6:7016–7025
- Wan ZQ, Jia CY, Yan W (2015) In situ growth of hierarchical NiS_2 hollow microspheres as efficient counter electrode for dye-sensitized solar cell. *Nanoscale* 7:12737–12742
- Hou WJ, Xiao YM, Han GY (2017) An interconnected ternary MIn_2S_4 ($\text{M}=\text{Fe}, \text{Co}, \text{Ni}$) thiospinel nanosheet array: a type of efficient platinum-free counter electrode for dye-sensitized solar cells. *Angew Chem Int Ed* 56:9146–9150

23. Khoo SY, Miao JW, Yang HB, He ZM, Leong KC, Liu B, Tan TTY (2015) One-step hydrothermal tailoring of NiCo_2S_4 nanostructures on conducting oxide substrates as an efficient counter electrode in dye-sensitized solar cells. *Adv Mater Interfaces* 2:1500384
24. Chen BK, Chang S, Li DY, Chen LL, Wang YT, Chen T, Zou BS, Zhong HZ, Rogach AL (2015) Template synthesis of CuInS_2 nanocrystals from In_2S_3 nanoplates and their application as counter electrodes in dye-sensitized solar cells. *Chem Mater* 27:5949–5956
25. Qian X, Liu HY, Yang JH, Wang HW, Huang J, Xu C (2019) Co–Cu– WS_x ball-in-ball nanospheres as high-performance Pt-free bifunctional catalysts in efficient dye-sensitized solar cells and alkaline hydrogen evolution. *J Mater Chem A* 7:6337–6347
26. He QQ, Qian TY, Zai JT, Qiao QQ, Huang SS, Li YR, Wang M (2015) Efficient Ag_8GeS_6 counter electrode prepared from nanocrystal ink for dye-sensitized solar cells. *J Mater Chem A* 3:20359–20365
27. Yan Q, Chang ML, Bao SJ, Bao QL (2007) Carbon nanotube/polyaniline composite as anode material for microbial fuel cells. *J Power Sources* 170: 79–84
28. Yue GT, Wu W, Liu XQ, Zheng HW (2018) Enhanced photovoltaic performance of dye-sensitized solar cells based on a promising hybrid counter electrode of $\text{CoSe}_2/\text{MWCNTs}$. *Sol Energy* 167:137–146
29. Liu XQ, Gao LF, Yue GT, Zheng HW, Zhang WF (2017) Efficient dye-sensitized solar cells incorporating hybrid counter electrode of CuMnSnS_4 microspheres/carbon nanotubes. *Sol Energy* 158:952–959
30. Yue GT, Wu JH, Xiao YM, Lin JM, Huang ML, Lan Z, Fan LQ (2013) Functionalized graphene/poly(3,4-ethylenedioxythiophene): polystyrenesulfonate as counter electrode catalyst for dye-sensitized solar cells. *Energy* 54:315–321
31. Cheng RZ, Gao XM, Yue GT, Fan LQ, Gao YY, Tan FR (2020) Synthesis of a novel MoIn_2S_4 alloy film as efficient electrocatalyst for dye-sensitized solar cell. *Sol Energy* 201:116–121
32. Qian X, Xu C, Jiang YQ, Zhang J, Guan GX, Huang YX (2019) Ni-Co- MoS_x ball-in-ball hollow nanospheres as Pt-free bifunctional catalysts for high-performance solar cells and hydrogen evolution reactions. *Chem Eng J* 368: 202–211
33. Senthilkumar R, Ramakrishnan S, Balu M, Ramamurthy PC, Kumaresan D, Kothurkar NK (2018) One-step hydrothermal synthesis of marigold flower-like nanostructured MoS_2 as a counter electrode for dye-sensitized solar cells. *J Solid State Electrochem* 22:3331–3341
34. Hou WJ, Xiao YM, Han GY (2018) The dye-sensitized solar cells based on the interconnected ternary cobalt diindium sulfide nanosheet array counter electrode. *Mater Res Bull* 107:204–212
35. Yue GT, Wu JH, Xiao YM, Huang ML, Lin JM, Lin JY (2013) High performance platinum-free counter electrode of molybdenum sulfide–carbon used in dye-sensitized solar cells. *J Mater Chem A* 1:1495–1501
36. Wu MX, Lin X, Wang YD, Wang L, Guo W, Qi DD, Peng XJ, Hagfeldt A, Grätzel M, Ma TL (2012) Economical Pt-free catalysts for counter electrodes of dye-sensitized solar cells. *J Am Chem Soc* 134:3419–3428
37. Liu XQ, Yue GT, Zheng HW (2017) A promising vanadium sulfide counter electrode for efficient dye-sensitized solar cells. *RSC Adv* 7:12474–12478
38. Ju MJ, Jeon I, Kim HM, Choi JI, Jung S, Seo J, Choi IT, Kang SH, Kim HS, Noh MJ (2016) Edge-selenated graphene nanoplatelets as durable metal-free catalysts for iodine reduction reaction in dye-sensitized solar cells. *Sci Adv* 56:e1501459

Publisher's Note

Springer Nature remains neutral with regard to jurisdictional claims in published maps and institutional affiliations.

Submit your manuscript to a SpringerOpen[®] journal and benefit from:

- Convenient online submission
- Rigorous peer review
- Open access: articles freely available online
- High visibility within the field
- Retaining the copyright to your article

Submit your next manuscript at ► [springeropen.com](https://www.springeropen.com)